2D Crystal engineering of nanosheets assembled from helical peptide building blocks

Merg, A.D.; Touponse, G.; Genderen, E. van; Zuo, X.B.; Bazrafshan, A.; Blum, T.; ... ; Conticello, V.P.

Citation

Note: To cite this publication please use the final published version (if applicable).

2D Crystal Engineering of Nanosheets Assembled from Helical Peptide Building Blocks

Andrea D. Merg, Gavin Touponse, Eric van Genderen, Xiaobing Zuo, Alisina Bazrafshan, Thorsten Blum, Spencer Hughes, Khalid Salaita, Jan Pieter Abrahams, and Vincent P. Conticello*

Abstract: *The successful integration of 2D nanomaterials into functional devices hinges on developing fabrication methods that afford hierarchical control across length scales of the entire assembly. We demonstrate structural control over a class of crystalline 2D nanosheets assembled from collagen triple helices. By lengthening the triple helix unit through sequential additions of Pro-Hyp-Gly triads, we achieved sub-angstrom tuning over the 2D lattice. These subtle changes influence the overall nanosheet size, which can be adjusted across the mesoscale size regime. The internal structure was observed by cryo-TEM with direct electron detection, which provides real-space high-resolution images, in which individual triple helices comprising the lattice can be clearly discerned. These results establish a general strategy for tuning the structural hierarchy of 2D nanomaterials that employ rigid, cylindrical structural units.*

Introduction

Owing to their ultrathin and planar geometry, two-dimensional (2D) nanoscale materials possess intrinsic physical properties that make them suitable for a diverse range of applications.[1] Inspired by the discovery of graphene and its unique properties,[2] numerous 2D nanomaterials of various compositions have been synthesized. However, systematic control of their structural hierarchy across a range of length scales remains a significant challenge. This is especially evident for bottom-up assembly methods for free-standing 2D nanostructures. Polymorphic assemblies are typically obtained, with little control over their lateral dimensions, which limits further material processing. Harvesting materials of pre-determined uniform sizes would streamline their incorporation into functional devices. Consequently, new assembly methods that afford hierarchical control over the entire assembled product (e.g. nano- to mesoscale) are critical for realizing their potential applications.

Recent 2D fabrication methods have employed sequence-programmable oligomers such as block copolymers,[3] peptides,[4] peptoids,[5] and nucleic acids.[6] Of these, peptides are extensively studied supramolecular building blocks. They possess excellent chemical diversity and predictable assembly behavior, which can be encoded through rational alterations to the primary structure.[7] However, the intrinsic chirality of amino acids and their proclivity toward unidirectional growth through H-bonding interactions precludes propagation in two dimensions. To circumvent this predisposition, researchers have utilized helical structural motifs (e.g., coiled coils, collagen triple helices, and alpha helices) to bias self-assembly in the lateral dimensions (Figure 1a).[4g–j] These structural units can be considered as "rigid rods." Programming interactions between the faces of these rod-like units can direct their lateral assembly.

By exploiting this design strategy, we have reported the construction of crystalline nanosheets assembled from collagen-mimetic peptides (CMPs).[4h,i] These peptides comprise three sequential blocks with positively charged, neutral, and negatively charged triads, and their folding into collagen triple helices facilitates their packing into a 2D lattice through Coulombic charge interactions between oppositely charged residues on adjacent triple helices (Figure 1b). The pristine and simple nanosheet construction leverages these materials as an ideal platform for studying how tuning the structural properties of helical building blocks influences the internal packing (nanoscale order) and overall assembly architecture (mesoscale order) for this material class. Understanding these factors will afford broad engineering principles for designing 2D assemblies that are constructed from rigid (super)helical structural motifs and provide a straightforward route for tailoring their structural properties.

Herein, we present a family of CMPs with varying numbers of canonical pro-triple helix forming Pro-Hyp-Gly triads comprising the central block (Figure 1c). We hypothesized that this series would provide a systematic level of understanding of the factor(s) that dictate structural changes of these 2D assembly systems involving rod-like protomers.

[*] Dr. A. D. Merg, G. Touponse, A. Bazrafshan, S. Hughes,
Prof. K. Salaita, Prof. V. P. Conticello
Department of Chemistry, Emory University
1515 Dickey Drive, Atlanta, GA 30322 (USA)
E-mail: vcontic@emory.edu

Dr. E. van Genderen, Dr. T. Blum, Prof. J. P. Abrahams
Paul Scherrer Institut, 5232 Villigen, PSI (Switzerland)

Dr. X. Zuo
X-ray Science Division, Argonne National Laboratory
9700 South Cass Avenue, Lemont, IL 60439 (USA)

Prof. J. P. Abrahams
Center for Cellular Imaging and NanoAnalytics, Biozentrum
University of Basel, 4058 Basel (Switzerland)
and
Leiden Institute of Biology
Sylviusweg 72, 2333 BE Leiden (The Netherlands)

Supporting information and the ORCID identification number(s) for the author(s) of this article can be found under:
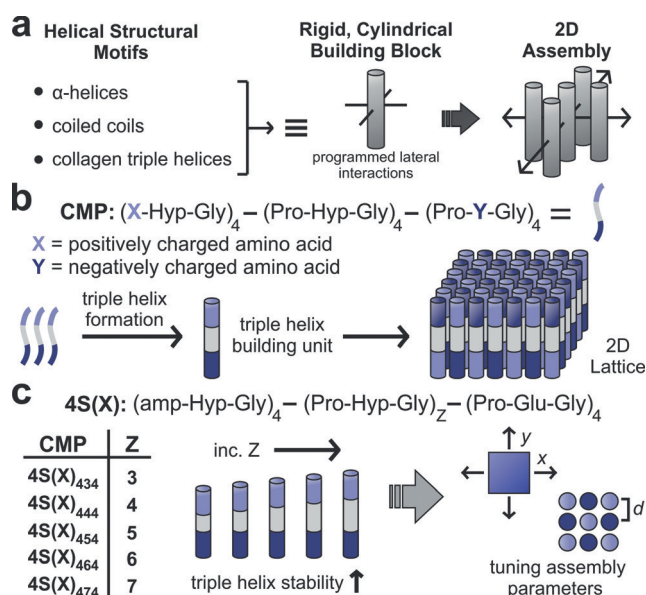https://doi.org/10.1002/anie.201906214.

Figure 1. a) 2D assemblies constructed from rigid helical peptide building blocks. b) Amino acid sequence of CMPs comprise positively charged, neutral, and negatively charged triads. Their folding into collagen triple helices gives rise to the triple helix building unit. Antiparallel packing of triple helices into a tetragonal 2D lattice is facilitated by the alignment of complementary charge interactions between adjacent triple helices. c) The 4S(X) peptide series with varying numbers (Z) of Pro-Hyp-Gly triads incorporated into the central block (amp = 4S-aminoproline). We hypothesize that incremental changes to CMP length may offer hierarchical control over the assembly parameters.

Increasing the peptide length would influence a variety of factors, in particular, triple-helix stability and the thickness of the resulting nanosheets, however, it was unclear as to whether it would influence lateral size and sheet dispersity.

Results and Discussion

CMPs were synthesized and purified using established methods and their compositions were confirmed by mass spectrometry (see Figures S1, S2 in the Supporting Information for details). Initial assembly experiments involved dissolving CMPs (4 mg mL^{-1}) in 20 mm 3-(N-morpholino)-propanesulfonic acid buffer (MOPS, pH 7.0), heating to 90 °C, and cooling to 4 °C or room temperature. The assemblies were allowed to assemble for 2 weeks.

Confirming our previous report, 4S(X)$_{444}$ (previously termed NSIII) assembles into square nanosheets of homogenous size at 4 °C (diagonal length, $L_d = 953 \pm 72$ nm; Figure 2 a,b).[4i] 4S(X)$_{454}$ assembles into smaller nanosheets ($L_d = 443 \pm 90$ nm) at room temperature (Figure 2 a,b). Their formation at room temperature is credited to the extra Pro-Hyp-Gly triad. 4S(X)$_{464}$ and 4S(X)$_{474}$ also assemble into nanosheets at room temperature, but the sheets appear to coalesce, forming larger "raft-like" assemblies (Figure S3). This could be due to the greater contour length associated with longer Pro-Hyp-Gly blocks, which may promote lateral interaction between the incipient nanosheets. To prevent raft formation, we repeated the assembly experiments at lower [CMP]. 4S(X)$_{464}$ and 4S(X)$_{474}$, assembled at 1 mg mL^{-1}, form
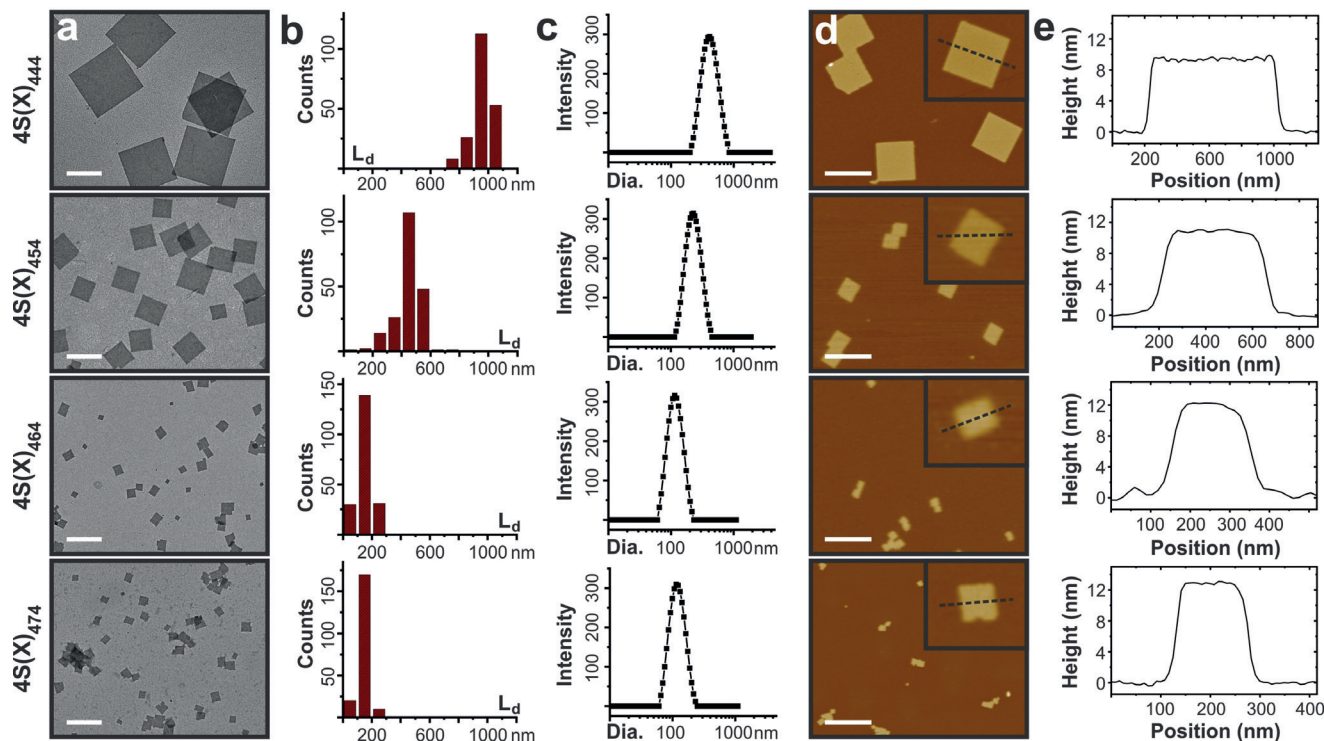
Figure 2. Characterization of 4S(X)$_{444}$, 4S(X)$_{454}$, 4S(X)$_{464}$, and 4S(X)$_{474}$ nanosheets a) TEM images (scale bar = 500 nm). b) L_d distribution of CMP nanosheets based on TEM (200 counts each). c) DLS spectra. d) AFM images (scale bar = 1 μm). e) Height trace of nanosheet shown in the inset of (d).

discrete nanosheets of similar dimensions ($L_d = 153 \pm 44$ nm and 149 ± 36 nm, respectively; Figure 2a,b). Finally, few nanosheets were observed for 4S(X)$_{434}$ at 4°C, which indicates that there is a threshold peptide length necessary for assembly to occur at this [CMP] (Figure S4). Doubling the concentration (8 mg mL^{-1}) yields polymorphic nanosheets in all dimensions, likely due to the high [CMP], and therefore we did not fully characterize their assembly (Figure S5). These results suggest that peptide concentration and assembly temperature have a significant influence on the optimal conditions for nanosheet formation, which may be interpreted in terms of these effects on triple helix stability.

The differences in sheet sizes observed by TEM was confirmed in situ using dynamic light scattering (DLS). Although, the Stokes–Einstein relationship is not valid for 2D assemblies, the population of nanosheets could still be fit to a single curve that is consistent with a uniform size distribution of self-assembled species (Figure 2c). DLS data confirm the decrease in sheet size with increasing Pro-Hyp-Gly repeats within the core block.

Atomic force microscopy (AFM) analysis of the nanosheets revealed sheet thicknesses of 9.4 ± 0.1 nm, 11.0 ± 0.3 nm, 11.9 ± 0.5 nm, and 12.8 ± 0.2 nm for 4S(X)$_{444}$, 4S-(X)$_{454}$, 4S(X)$_{464}$, and 4S(X)$_{474}$ sheets, respectively (Figure 2d,e and Figures S6, S7). These measurements agree with theoretical thicknesses of 10.3 nm, 11.2 nm, 12.0 nm, and 12.9 nm (0.286 nm rise/residue for collagen triple helices).[8] The heights obtained from AFM confirm that the nanosheets comprise a single layer with triple helices packed perpendicular to the surface. Altogether, these results demonstrate that one can systematically tune CMP nanosheets in all dimensions simply through extending the length of the triple helical building block.

Circular dichroism (CD) spectropolarimetry of CMP nanosheets shows the characteristic collagen triple helix profile marked by a positive maximum at approximately 224 nm and a negative minimum at approximately 198 nm (Figure 3). Rpn values, which report the ratio of these peak intensities, is useful in determining the formation of collagen triple helices in solution.[9] The values confirm that the triple
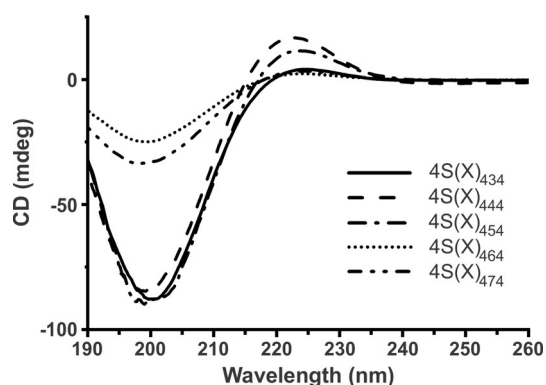
helices are present for all optimized CMP assemblies (Rpn ≥ 0.09) except for 4S(X)$_{434}$ (4 mg mL^{-1}, Rpn = 0.05).[9]

It is well-known that increasing the Pro-Hyp-Gly length within collagen peptides increases the stability of the triple helix.[10] Thermal denaturation studies of 4S(X)$_{444}$, 4S(X)$_{454}$, 4S(X)$_{464}$, and 4S(X)$_{474}$ sheets revealed melting temperatures (T_m) of 34°C, 50°C, 44°C, and 49°C, respectively (Figure S8). The lower T_m of 4S(X)$_{464}$ and 4S(X)$_{474}$ compared to 4S(X)$_{454}$ is attributed to the lower [CMP]. In order to allow direct comparison of the triple helix stability between CMPs, T_m measurements were acquired on pre-assembled CMP nanosheets at a single concentration (1 mg mL^{-1}; Figure S9). Thermal transitions at 22°C and 37°C for 4S(X)$_{444}$ and 4S(X)$_{454}$, respectively, provide further evidence that shorter CMPs with fewer Pro-Hyp-Gly triads are less stable than their longer CMP counterparts.

We hypothesized that the change in size over the 4S(X) series is likely due to the frequency of nucleation events that occur during the assembly process. Moreover, TEM data reveal differences in sheet homogeneity between CMP assemblies. To address these discrepancies, timepoint studies were conducted (Figure 4a and Figures S10–12). Small 4S-(X)$_{444}$ nanosheets are observed as early as 30 min after reaching the incubation temperature of 4°C. Subsequent timepoints reveal that the sheets appear to grow uniformly and reach maturity after 2 weeks (Figure 4a). Similarly, 4S(X)$_{454}$, 4S(X)$_{464}$, and 4S(X)$_{474}$ nanosheets are observed at early timepoints at room temperature and grow over time;
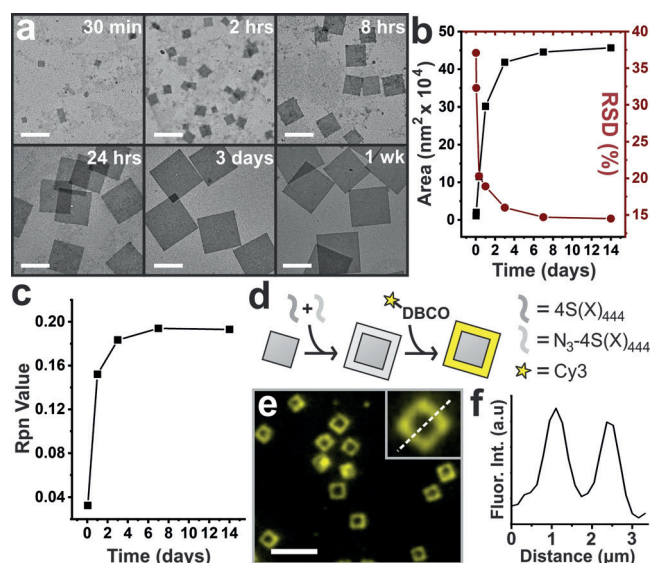

Figure 4. a) TEM images of 4S(X)$_{444}$ nanosheets at various timepoints over the first week of assembly at 4°C. Scale bar = 500 nm. b) Square area of 4S(X)$_{444}$ nanosheets and corresponding RSD values as a function of assembly time. c) Rpn values of 4S(X)$_{444}$ assembly solution as a function of assembly time. d) Homoepitaxial growth of 4S(X)$_{444}$ and N$_3$-4S(X)$_{444}$ monomers (9:1) around preformed 4S(X)$_{444}$ sheets followed by attachment of Cy3 via copper-free azide–alkyne cycloaddition. e) Fluorescence optical micrograph after 1 week of growth reveals the successful homoepitaxy off 4S(X)$_{444}$ nanosheet seeds. Scale bar = 5 μm. False color is used to enhance contrast. f) Fluorescence line scan of the nanosheet shown in the inset of (e).

Figure 3. CD spectra of assembly solutions of 4S(X)$_{434}$ (4 mg mL^{-1}, Rpn = 0.05); 4S(X)$_{444}$ (4 mg mL^{-1}, Rpn = 0.19); 4S(X)$_{454}$ (4 mg mL^{-1}, Rpn = 0.13); 4S(X)$_{464}$ (1 mg mL^{-1}, Rpn = 0.09); 4S(X)$_{474}$ (1 mg mL^{-1}, Rpn = 0.10).

however, the sheets appear to be less homogenous throughout the assembly process (Figures S10–12).

To quantify these results, we plotted nanosheet size as a function of time along with the corresponding relative standard deviation (RSD; Figure 4b and Figure S13). RSD values were calculated to determine the degree of dispersity of the sheet population. Sheets grew in a logarithmic fashion regardless of CMP length. A starting RSD value of 37% was observed for $4S(X)_{444}$, followed by an exponential decrease in a manner that is inversely proportional to growth in sheet size (Figure 4b). The decrease in RSD values implies that no sheet nucleation occurs after the initial nucleation event. As the sheets grow, the difference in sheet sizes become less significant, leading to smaller RSD values.

In contrast, the RSD values for $4S(X)_{454}$, $4S(X)_{464}$, and $4S(X)_{474}$ nanosheets over the 2-week time study remain relatively constant, thus suggesting that nanosheet seeds continue forming throughout the assembly process (Figure S13). Analysis of distribution data for sheet sizes collected at each timepoint confirmed the assembly discrepancies between CMPs (Figure S14). While monodisperse nanosheet seeds are formed within 2 hrs for all CMPs, frequent nucleation events for $4S(X)_{464}$ and $4S(X)_{474}$ assemblies continue to take place throughout the assembly process. $4S(X)_{444}$ seeds, however, are almost exclusively formed during the initial nucleation event (within 2 hrs). The initial nanosheets generated at these early timepoints serve as seeds for homoepitaxial addition of collagen triple helices. $4S(X)_{454}$ follows a similar assembly process as $4S(X)_{444}$, however, sheet nucleation continues to occur after the initial timepoints, although less frequently than with the longer CMPs.

In addition to TEM, CD timepoint studies were also conducted to monitor the formation of collagen triple helices in solution (Figure S15). Interestingly, the Rpn values, which provide feedback on triple helix formation, increase over time in a manner comparable to sheet growth, thus implying that sheet growth is controlled by triple helix formation or vice versa (Figure 4c and Figure S16). This codependence may be due to the stabilization of triple helix folding offered by the 2D lattice of the nanosheet assembly, which counteracts the unfavorable charge repulsion between parallel strands within isolated CMP triple helices.

From these time-dependent studies, we conclude that the homogeneity and lateral dimensions of nanosheets are nucleation-dependent, and that tuning the length of the central block regulates the generation of sheet nuclei, which controls sheet size and dispersity. We hypothesize that $4S(X)_{444}$ happens to be at the "sweet spot", that is, the position in which nucleation of the sheets and subsequent growth off those sheets is controlled, which gives rise to unusually monodisperse nanosheets. The assembly process resembles crystallization-driven living polymerization, where seed edges remain active to epitaxial growth of successive additions of monomers.[3e, 11] To probe whether $4S(X)_{444}$ nanosheets are "living," a 9:1 mixture of $4S(X)_{444}$ and N-terminal azido-modified $4S(X)_{444}$ (azido-PEG5-acid, N_3–4S-$(X)_{444}$; Figure S17) monomers were introduced to a solution of pre-assembled $4S(X)_{444}$ nanosheets. The azide derivative allows the postsynthetic conjugation of Cy3 fluorophore onto

the sheet surface through copper-free azide–alkyne cyclo-addition (Figure 4d). TEM and Fluorescence microscopy of nanosheets after 1 week reveals the successful homoepitaxy (Figure 4e,f and Figures S18,S19), unveiling an additional route for fabricating size-tunable CMP nanosheets as well as highlighting the potential for functionalizing the sheet surface with nanoscale spatial control. In summary, we reason that $4S(X)_{444}$ has a diminished ability to generate new nuclei compared to the more crystallizable triple helices of longer CMPs. This allows a controlled growth process where newly formed triple helices attach onto existing nanosheets leading to a more uniform product.

Small- and wide-angle X-ray scattering (SAXS/WAXS) experiments were conducted on the nanosheets to characterize their internal structure. We hypothesized that differences in lattice packing parameters and degree of crystallinity could contribute to the observed variation in sheet size. Scattering curves were obtained for all CMP nanosheets, including $4S(X)_{434}$ nanosheets (8 mg mL^{-1}; Figure 5a, Table 1). The scattering intensities at low q region ($q < 0.02$ Å^{-1}) roughly follow q^{-2} power law, indicating a uniform sheet-like morphology for all CMP nanosheets except those derived from $4S(X)_{434}$, which is likely due to multilamellar stacking. Fitting
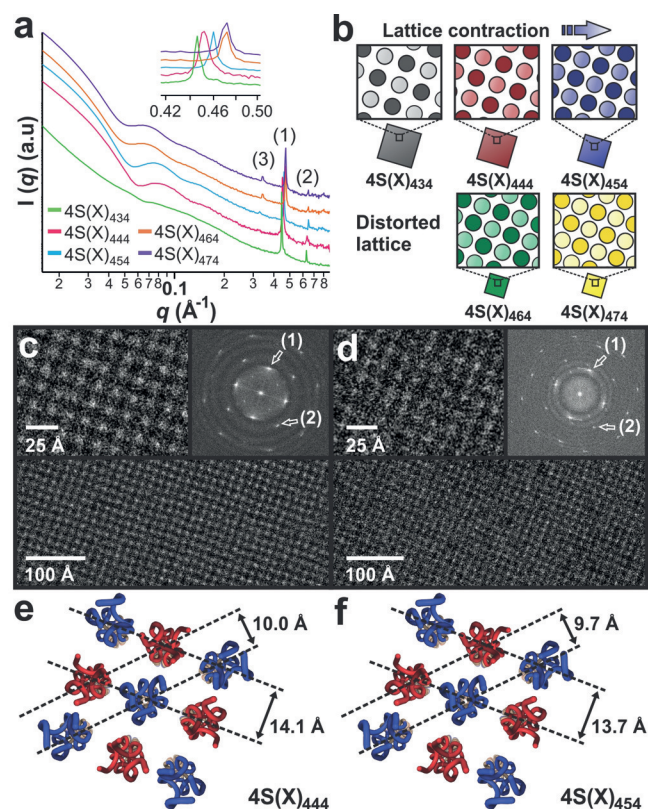

Figure 5. a) Synchrotron SAXS scattering profile (see Table 1 for *d*-spacings). Inset: expansion of peak (1) diffraction peaks. b) Cartoon representations of the different lattice packing parameters of collagen triple helices (colored circles) between CMP nanosheets. c,d) High-resolution cryo-TEM images and corresponding FFT analysis of $4S(X)_{444}$ (c) and $4S(X)_{454}$ (d) nanosheets. FFT spots (*d*-spacing) for $4S(X)_{444}$: (1) 14.1 Å, 10.0 Å and $4S(X)_{454}$: (1) 13.7 Å, (2) 9.7 Å. e,f) Assembly model of the 2D lattice of $4S(X)_{444}$ (e) and $4S(X)_{454}$ (d) nanosheets.

Table 1: Calculated *d*-spacings (Å) of Bragg peaks obtained from SAXS.

Peak Number	4S(X)$_{434}$	4S(X)$_{444}$	4S(X)$_{454}$	4S(X)$_{464}$	4S(X)$_{474}$
(1)	14.1	13.9	13.7	13.4	13.3
(2)	10.0	9.9	9.7	9.7	9.7
(3)	–	–	19.2	18.5	18.5

the low *q* data using the Guinier equation for sheet-like forms gives average sheet thicknesses that are consistent with AFM and theoretical height calculations (105.9 Å, 119.3 Å, 128.5 Å, 134.7 Å; Figure S20). The oscillations in the *q* region of approximately 0.03–0.3 Å^{-1} arise from the thickness of the nanosheets and the attenuation of the oscillation reflects the variation of nanosheet thickness, which is estimated as around 15 Å (Figure S21).[4i]

All CMP nanosheets possess a high degree of crystallinity as observed from the presence of several Bragg diffraction peaks in the high *q* region (i.e., small *d*-spacing) of the intensity plot (Figure 5 a). Unsurprisingly, the peak patterns are comparable, thus indicating that they exhibit a similar underlying assembly structure. Peaks (1) and (2), observed for all CMP sheets, correspond to *d*-spacings that range from 14.1 Å to 13.3 Å and 10.0 Å to 9.7 Å (Table 1). These sets of peaks are related in that peak (2) multiplied by $\sqrt{2}$ is roughly equal to peak (1), which suggests the presence of ordered tetragonal packing of collagen triple helices within the assemblies. This relation holds well for 4S(X)$_{444}$ and 4S(X)$_{454}$ nanosheets, but to a lesser extent for nanosheets derived from 4S(X)$_{464}$ and 4S(X)$_{474}$, thus implying that the tetragonal lattices of the latter are slightly distorted. Furthermore, the results reveal that the lattice contracts with each Pro-Hyp-Gly addition to the core block (Figure 5 b). We note that the WAXS data for 4S(X)$_{444}$ are slightly different than that previously reported.[4i] We ascribe these differences to the previously reported sheets not having reached full maturity.

The SAXS/WAXS data suggest that the longer CMP sequences allow the protomers to pack more tightly to one another within the 2D lattice. Close examination of peak (3), found at smaller *q* values, reveals that this peak becomes more prominent with increasing CMP length, which is a sign that the nanosheet exhibits greater internal crystallinity at longer length scales. Moreover, the lattice distortion observed for 4S(X)$_{464}$ and 4S(X)$_{474}$ is reminiscent of single-crystal X-ray diffraction studies of synthetic collagen triple helices, which often pack into layered structures displaying distorted pseudo-tetragonal or hexagonal packing symmetry.[12] We hypothesize that as the central block becomes longer, its structure increasingly dominates the 2D packing behavior of the triple helices, which deviates from a purely tetragonal lattice. Altogether, these results correspond well with the previous results in that longer CMPs generate sheet nuclei more readily than their shorter CMP counterparts.

Cryogenic transmission electron microscopy (cryo-TEM) with direct electron detection was employed on 4S(X)$_{444}$ and 4S(X)$_{454}$ nanosheets to study their internal structure in further detail (Figure 5 c,d and Figures S22, S23). These peptides were chosen as substrates because the larger size of the corre-

sponding nanosheets facilitates visualization under the microscope. High-resolution cryo-TEM images reveal strikingly ordered tetragonal packing of individual triple helices within the nanosheet assembly, in which individual distances between triple helical protomers can be determined directly in real space.

Fast Fourier transformations (FFTs) of the cryo-TEM images confirm the high degree of order within the nanosheets, with Bragg spots observed up to *d*-spacings of around 4.5 Å (Figures S22, S23). The presence of Thon rings at resolutions outside the computed Bragg spots indicates the breakdown of 2D order beyond that resolution. A 4-fold rotational symmetry confirms the tetragonal lattice of both CMP assemblies. Measured *d*-spacings of approximately 14.1 Å and 10.0 Å for 4S(X)$_{444}$ nanosheets, and approximately 13.7 Å and 9.7 Å for 4S(X)$_{454}$ nanosheets are in close agreement with corresponding *d*-spacings obtained from the 1D SAXS curves. To account for any distortions of Bragg spots arising from their possible location on Thon rings, images obtained with similar defocus distances were used to allow direct comparison.

Based on the structural information obtained from AFM, SAXS, and cryo-TEM, we propose assembly models for 4S(X)$_{444}$ and 4S(X)$_{454}$ nanosheets (Figure 5 e,f). The nanosheets comprise a single 2D tetragonal lattice of collagen triple helices that are oriented perpendicular to the sheet surface. The helices pack in an antiparallel fashion, thereby allowing oppositely charged triads from neighboring triple helices to be in contact, which provides the cohesive electrostatic interactions that stabilize the triple helices and the corresponding 2D assemblies. We note that the model for 4S(X)$_{444}$ sheets corrects a previously proposed model,[4i] which highlights the importance of real-space imaging obtainable by cryo-TEM compared to SAXS measurements in which the data are azimuthally averaged. Furthermore, we can propose a model for 4S(X)$_{434}$ nanosheets, which is simply an expansion of the 4S(X)$_{444}$ lattice. While at present, assembly models for 4S(X)$_{464}$ and 4S(X)$_{474}$ assemblies cannot be constructed with full certainty, the insight obtained from this study allows us to propose that their lattices are nearly identical and are slightly distorted and contracted compared to the rest of the 4S(X) family. These structural distortions may reflect the intrinsic packing preference of the longer Pro-Hyp-Gly block within the triblock sequence architecture (see above).

Conclusion

In conclusion, we demonstrate hierarchical structural control of nanosheets through systematic changes to the triple helix architecture. We show that sequence-directed self-assembly of cylindrical rod-like units, such as collagen triple helices, is a facile mechanism for the construction of structurally defined and tunable 2D assemblies. The results suggest that supramolecular interactions between structural elements can be propagated hierarchically to afford structural control across length-scales. Furthermore, we demonstrate homoepitaxial growth of 4S(X)$_{444}$ nanosheets, which highlights an intriguing handle for incorporating multiple func-

tional domains within the assembly architecture with nano-scale resolution. Finally, we anticipate that these results will afford general assembly guidelines for engineering 2D systems that are built from rigid, helical structural motifs and offer instruction for controlling their assembly parameters across a range of length-scales.

Conflict of interest

The authors declare no conflict of interest.

[1] a) H. Zhang, *ACS Nano* **2015**, *9*, 9451–9469; b) X. Zhuang, Y. Mai, D. Wu, F. Zhang, X. Feng, *Adv. Mater.* **2015**, *27*, 403–427; c) T. Govindaraju, M. B. Avinash, *Nanoscale* **2012**, *4*, 6102–6117; d) C. E. Boott, A. Nazemi, I. Manners, *Angew. Chem. Int. Ed.* **2015**, *54*, 13876–13894; *Angew. Chem.* **2015**, *127*, 14082–14101; e) J. W. Colson, W. R. Dichtel, *Nat. Chem.* **2013**, *5*, 453; f) S. Zhang, J. Zhang, W. Fang, Y. Zhang, Q. Wang, J. Jin, *Nano Lett.* **2018**, *18*, 6563–6569; g) C.-A. Palma, P. Samorì, *Nat. Chem.* **2011**, *3*, 431; h) X. Zhang, Y. Xie, *Chem. Soc. Rev.* **2013**, *42*, 8187–8199; i) J. Sakamoto, J. van Heijst, O. Lukin, A. D. Schlüter, *Angew. Chem. Int. Ed.* **2009**, *48*, 1030–1069; *Angew. Chem.* **2009**, *121*, 1048–1089.

[2] K. S. Novoselov, A. K. Geim, S. V. Morozov, D. Jiang, Y. Zhang, S. V. Dubonos, I. V. Grigorieva, A. A. Firsov, *Science* **2004**, *306*, 666–669.

[3] a) L. Han, M. Wang, X. Jia, W. Chen, H. Qian, F. He, *Nat. Commun.* **2018**, *9*, 865; b) X. He, M.-S. Hsiao, C. E. Boott, R. L. Harniman, A. Nazemi, X. Li, M. A. Winnik, I. Manners, *Nat. Mater.* **2017**, *16*, 481; c) A. Nazemi, X. He, L. R. MacFarlane, R. L. Harniman, M.-S. Hsiao, M. A. Winnik, C. F. J. Faul, I. Manners, *J. Am. Chem. Soc.* **2017**, *139*, 4409–4417; d) H. Qiu, Y. Gao, C. E. Boott, O. E. C. Gould, R. L. Harniman, M. J. Miles, S. E. D. Webb, M. A. Winnik, I. Manners, *Science* **2016**, *352*, 697; e) B. Yu, X. Jiang, J. Yin, *Macromolecules* **2014**, *47*, 4761–4768; f) M. Inam, G. Cambridge, A. Pitto-Barry, Z. P. L. Laker, N. R. Wilson, R. T. Mathers, A. P. Dove, R. K. O'Reilly, *Chem. Sci.* **2017**, *8*, 4223–4230.

[4] a) H.-S. Jang, J.-H. Lee, Y.-S. Park, Y.-O. Kim, J. Park, T.-Y. Yang, K. Jin, J. Lee, S. Park, J. M. You, K.-W. Jeong, A. Shin, I.-S. Oh, M.-K. Kwon, Y.-I. Kim, H.-H. Cho, H. N. Han, Y. Kim, Y. H. Chang, S. R. Paik, K. T. Nam, Y.-S. Lee, *Nat. Commun.* **2014**, *5*, 3665; b) J. Lee, I. R. Choe, N.-K. Kim, W.-J. Kim, H.-S. Jang, Y.-S. Lee, K. T. Nam, *ACS Nano* **2016**, *10*, 8263–8270; c) Y. Lin, M. R. Thomas, A. Gelmi, V. Leonardo, E. T. Pashuck, S. A. Maynard, Y. Wang, M. M. Stevens, *J. Am. Chem. Soc.* **2017**, *139*, 13592–13595; d) B. Dai, D. Li, W. Xi, F. Luo, X. Zhang, M. Zou, M. Cao, J. Hu, W. Wang, G. Wei, Y. Zhang, C. Liu, *Proc. Natl. Acad. Sci. USA* **2015**, *112*, 2996–3001; e) A. S. Parmar, J. K. James, D. R. Grisham, D. H. Pike, V. Nanda, *J. Am. Chem. Soc.* **2016**, *138*, 4362–4367; f) I. W. Hamley, A. Dehsorkhi, V. Castelletto, *Chem. Commun.* **2013**, *49*, 1850–1852; g) H. V. Zhang, F. Polzer, M. J. Haider, Y. Tian, J. A. Villegas, K. L. Kiick, D. J. Pochan, J. G. Saven, *Sci. Adv.* **2016**, *2*, e1600307; h) T. Jiang, C. Xu, Y. Liu, Z. Liu, J. S. Wall, X. Zuo, T. Lian, K. Salaita, C. Ni, D. Pochan, V. P. Conticello, *J. Am. Chem. Soc.* **2014**, *136*, 4300–4308; i) T. Jiang, C. Xu, X. Zuo, V. P. Conticello, *Angew. Chem. Int. Ed.* **2014**, *53*, 8367–8371; *Angew. Chem.* **2014**, *126*, 8507–8511; j) E. L. Magnotti, S. A. Hughes, R. S. Dillard, S. Wang, L. Hough, A. Karumbamkandathil, T. Lian, J. S. Wall, X. Zuo, E. R. Wright, V. P. Conticello, *J. Am. Chem. Soc.* **2016**, *138*, 16274–16282.

[5] a) E. J. Robertson, A. Battigelli, C. Proulx, R. V. Mannige, T. K. Haxton, L. Yun, S. Whitelam, R. N. Zuckermann, *Acc. Chem. Res.* **2016**, *49*, 379–389; b) E. J. Robertson, G. K. Olivier, M. Qian, C. Proulx, R. N. Zuckermann, G. L. Richmond, *Proc. Natl. Acad. Sci. USA* **2014**, *111*, 13284–13289; c) H. Jin, F. Jiao, M. D. Daily, Y. Chen, F. Yan, Y.-H. Ding, X. Zhang, E. J. Robertson, M. D. Baer, C.-L. Chen, *Nat. Commun.* **2016**, *7*, 12252; d) K. T. Nam, S. A. Shelby, P. H. Choi, A. B. Marciel, R. Chen, L. Tan, T. K. Chu, R. A. Mesch, B.-C. Lee, M. D. Connolly, C. Kisielowski, R. N. Zuckermann, *Nat. Mater.* **2010**, *9*, 454.

[6] a) Y. He, Y. Chen, H. Liu, A. E. Ribbe, C. Mao, *J. Am. Chem. Soc.* **2005**, *127*, 12202–12203; b) W. Liu, H. Zhong, R. Wang, N. C. Seeman, *Angew. Chem. Int. Ed.* **2011**, *50*, 264–267; *Angew. Chem.* **2011**, *123*, 278–281; c) P. Wang, S. Gaitanaros, S. Lee, M. Bathe, W. M. Shih, Y. Ke, *J. Am. Chem. Soc.* **2016**, *138*, 7733–7740; d) H. Yu, D. T. L. Alexander, U. Aschauer, R. Häner, *Angew. Chem. Int. Ed.* **2017**, *56*, 5040–5044; *Angew. Chem.* **2017**, *129*, 5122–5126.

[7] A. Lampel, R. V. Ulijn, T. Tuttle, *Chem. Soc. Rev.* **2018**, *47*, 3737–3758.

[8] a) K. Okuyama, *Connect. Tissue Res.* **2008**, *49*, 299–310; b) K. Okuyama, X. Xu, M. Iguchi, K. Noguchi, *Peptide Sci.* **2006**, *84*, 181–191.

[9] Y. Feng, G. Melacini, J. P. Taulane, M. Goodman, *J. Am. Chem. Soc.* **1996**, *118*, 10351–10358.

[10] A. V. Persikov, J. A. M. Ramshaw, B. Brodsky, *J. Biol. Chem.* **2005**, *280*, 19343–19349.

[11] a) Z. M. Hudson, C. E. Boott, M. E. Robinson, P. A. Rupar, M. A. Winnik, I. Manners, *Nat. Chem.* **2014**, *6*, 893; b) J. B. Gilroy, T. Gädt, G. R. Whittell, L. Chabanne, J. M. Mitchels, R. M. Richardson, M. A. Winnik, I. Manners, *Nat. Chem.* **2010**, *2*, 566.

[12] a) K. Okuyama, C. Hongo, G. Wu, K. Mizuno, K. Noguchi, S. Ebisuzaki, Y. Tanaka, N. Nishino, H. P. Bächinger, *Biopolymers* **2009**, *91*, 361–372; b) K. Okuyama, K. Miyama, K. Mizuno, H. P. Bächinger, *Biopolymers* **2012**, *97*, 607–616; c) C. Hongo, K. Noguchi, K. Okuyama, Y. Tanaka, N. Nishino, *J. Biochem.* **2005**, *138*, 135–144; d) R. Berisio, L. Vitagliano, L. Mazzarella, A. Zagari, *Protein Sci.* **2002**, *11*, 262–270.